第 41 卷 第 3 期
2026 年 6 月

新型炭材料（中英文）
New Carbon Materials

Electrochemically activated NiOOH/NiFeV-LDH@CC for a highly efficient oxygen evolution reaction

Song Yujie[1], Yue Yunfei[1], Shen Zhichao[1], Hou Ying[1], Song Yanhui[1],
Liu Peizhi[1], Xu Bingshe[1,2], Zhang Haixia[1,*], Guo Junjie[1,*]
(1. *Key Laboratory of Interface Science and Engineering in Advanced Materials Ministry of Education, Taiyuan University of Technology, Taiyuan* 030024, *Shanxi*, *China*;
2. *Materials Institute of Atomic and Molecular Science*, *Shaanxi University of Science* & *Technology*, *Xi'An* 710021, *Shaanxi*, *China*)

Abstract: The surface reconstruction of NiFe-based layered double hydroxide (LDH) electrocatalysts has been widely studied. The reconstructed NiOOH phase plays a critical role in improving the oxygen evolution reaction (OER) performance of NiFe-based LDHs, but observing the NiOOH phase is difficult because of its instability and exploring the functional mechanism of NiOOH in NiFe-based LDHs remains a great challenge. A simple electrochemical activation was used to synthesize a NiOOH/NiFeV-LDH@CC catalyst consisting of an array of V-doped NiFe-LDH nanosheets on carbon cloth (CC), in which the reconstructed NiOOH phase is the active species. During electrochemical activation, the release of doped V leads to the formation of abundant vanadium vacancy (V_V) and oxygen vacancy (V_O) species, and thus the surface of the NiFe-LDH nanosheets is reconstructed to form NiOOH. Because of the improved intrinsic activity from the NiOOH active phase, and the increased electrical conductivity produced by the abundant V_O, NiOOH/NiFeV-LDH@CC has an excellent OER performance in an alkaline solution, with low overpotentials of 209 mV and 241 mV at 20 mA cm^{-2} and 100 mA cm^{-2}, respectively. It also has a long-term stability of 80,000 s at a constant current density of 10 mA cm^{-2}. Using NiOOH/NiFeV-LDH@CC as the anode, an assembled over water splitting (OWS) battery can drive a current density of 20 mA cm^{-2} (without iR compensation) at a much lower voltage of 1.597 V. At the same time, the electrolytic cell can deliver a current density of 10 mA cm^{-2} at ~ 1.55V for more than 80,000 s without significant loss. This electrochemical activation method can be used in future designs of electrocatalysts for OER.

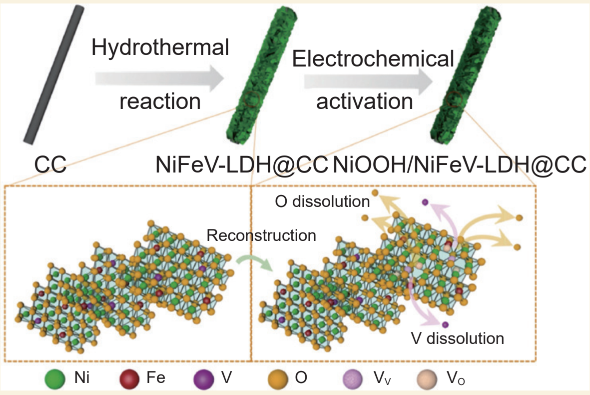

Key words: V doping；NiFe-based Layered double hydroxides；Electrochemical reconstruction；NiOOH；Oxygen evolution reaction

1 Introduction

The reliance on fossil fuels since the Industrial age has resulted in the emission of carbon dioxide, which causes global warming. With the objective of achieving Net Zero, hydrogen is considered an ideal substitute for its high specific energy density, regenerative, and pollution-free properties[1]. Hydrogen production from water electrolysis is the most promising method due to its abundant source of reactants, relatively mature process and environmental friendliness. During electrolysis, oxygen evolution reaction (OER) at the anode suffers from poor efficiency and high kinetic barrier due to having a four-electron coupled process and complicated intermediate reaction[2–4]. The difficulties can be overcome using high-performance electrocatalysts. At present, Ir- and Ru-based electrocatalysts such as IrO_2 and RuO_2 show good OER performance, but their high price and scarcity in the earth's crust hinder the adoption of hydrogen to

Received: January 05, 2026
Revised: April 04, 2026
Accepted: April 05, 2026

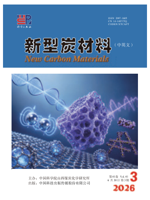

replace fossil fuels[5–8]. Therefore, the discovery and research for inexpensive and easily prepared non-noble metal electrocatalysts for efficient and stable OER is becoming increasingly important[9].

Transition metal-based compounds such as transition metal oxides[1,10–11], phosphides[12–15], sulphides[16–18] and hydroxides[19–22] are considered as candidates for OER electrocatalysts. Among these, layered double hydroxides (LDHs) are a type of transition metal-based electrocatalyst that consists of layers of divalent and trivalent metal cations coupled to hydroxide anions, with the guest anion wedged between the layers[19–20,23–24]. NiFe-based LDHs have efficient OER performance in alkaline solution[25]. The valence of Ni increases from 2+ to 3+ under an applied electric field, leading to the surface reconstruction of NiFe-based LDHs during OER. The formation of NiOOH phase indicates the true active phase of NiFe-based LDHs[26]. The impact of surface reconstruction on the OER performance of NiFe-based LDHs electrocatalysts has been verified by researchers. Zhai et al. studied ways to promote the generation of reconstructed NiOOH active species in NiFe-LDH materials with the synergistic effect of O vacancies (V_O) and Fe vacancies (V_{Fe}) by in-situ Raman. This effect serves to enhance the OER performance of NiFe-LDH and optimizing the adsorption free energy of oxygen-containing intermediates[27]. Chen et al. reported that Zn vacancies (V_{Zn}) in Zn-doped NiFeP nanosheets caused by the removal of Zn ions promoted the formation of the reconstructed NiOOH phase, improving the OER performance of Zn-doped NiFeP nanosheets[28]. Wu et al. explored the influence of metal vacancies (V_{Ni} and V_{Fe}) on the surface reconstruction of NiFe-LDHs by in-situ Raman, and concluded that the real active species in the OER process is thought to be the reconstructed NiOOH phase[29]. It can be seen in literature that reconstructed NiOOH phase often enhances the electrocatalyst' OER performance. However, said phase is unstable and difficult to be observed directly. The precise mechanism of NiOOH in NiFe-based LDHs during OER remains unclear[30].

Vanadium (V) with 3d outer electron characteristics has recently emerged as a promising material in the field of water-splitting electrocatalysts[26]. Thanks to its abundant natural reserves, low cost, and flexible oxidation states (ranging from +2 to +5, which enables strong electronic interactions with other metal cations), the incorporation of V is beneficial for introducing vacancy defects and promoting the reconstruction of NiFe-LDHs, thus enhancing the intrinsic catalytic activity and structural flexibility[26]. Herein, a V-doped NiFe-LDH catalyst with the structure of 2D nanosheet array on carbon cloth (CC) is synthesized (NiOOH/NiFeV-LDH@CC) by a two-step method of hydrothermal reaction followed by in-situ electrochemical activation (Fig. 1), in which the reconstructed NiOOH phase as the actual active species is formed due to abundant V vacancies (V_V) and V_O from the release of doped V during the redox process. Benefiting from the NiOOH active phase on the surface of NiFeV-LDH@CC, NiOOH/NiFeV-LDH@CC exhibits excellent OER performance in 1 mol L^{-1} KOH solution, requiring an overpotential as low as 209 mV to drive a current density of 20 mA cm^{-2}. This method can be extended to other NiFe-based materials to enhance their electrocatalytic activity and study the transformation process.

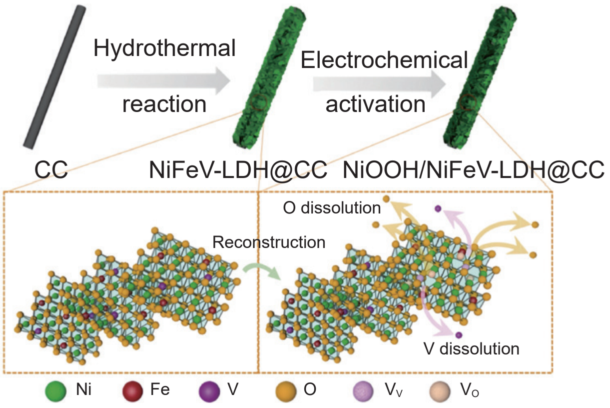

Fig. 1 Schematic illustration of the manufacturing of NiOOH/NiFeV-LDH@CC

2 Materials and methods

2.1 Materials

Nickel nitrate hexahydrate ($Ni(NO_3)_2 \cdot 6H_2O$, AR), iron nitrate nonahydrate ($Fe(NO_3)_3·9H_2O$, AR), vanadium trichloride (VCl_3, 99%) were purchased from Anhui Senrise Technology Co., Ltd. Ammonium fluoride (NH_4F, 99.99%), urea ($CO(NH_2)_2$, 99%) and potassium hydroxide (KOH, 95%) were purchased from Shanghai Aladdin Biochemical Technology Co., Ltd. Ruthenium (IV) oxide (RuO_2, 99.9%) and 20% Pt/C (99.9%) were bought from Alfa Aesar. Acetone (CH_3OH), Ethanol (C_2H_5OH, AR) were purchased from Damao Chemical Reagent Factory. All chemicals were used as is without additional purification. Carbon cloth (CC) was bought from Cetech Co., Ltd.

2.2 Material synthesis

2.2.1 Pretreatment of CC

In order to remove impurities on the surface of CC and improve its wettability, CC was cut into 1 cm × 3 cm strips and cleaned ultrasonically in CH_3OH, C_2H_5OH, and deionized (DI) water, successively for 10 mins each, then dried at 60 °C for 12 h.

2.2.2 Preparation of NiFeV-LDH@CC

The NiFeV-LDH@CC nanosheets were fabricated with a hydrothermal process. Typically, a precursor solution was obtained by mixing 2 mmol of $Ni(NO_3)_2·6H_2O$, 0.25 mmol of $Fe(NO_3)_3·9H_2O$, 0.125 mmol of VCl_3, 10 mmol of $CO(NH_2)_2$ and 6 mmol NH_4F with 35 mL DI water and stirred until homogeneous. The precursor solution and the treated CC were put into a 50 mL Teflon-lined autoclave and stirred. The autoclave was maintained at 160 ºC for 6 h. Following which, the products were taken out and rinsed 3 times with DI water and C_2H_5OH before being vacuum-dried at 60 °C overnight. We also prepared $NiFeV_{0.25}$-LDH@CC in the same way as the compared sample, with the sole exception being an additional 0.25 mmol VCl_3.

2.2.3 Preparation of NiOOH/NiFeV-LDH@CC

NiOOH/NiFeV-LDH@CC was made from NiFeV-LDH@CC with chemical activation. A Saturated Calomel Electrode (SCE, filled with saturated KCl solution) and a carbon rod (6 mm in diameter) were utilized as a reference electrode and a counter electrode. Platinum electrode clip clamped NiFeV-LDH@CC on CC was used as the working electrode with a working area of 1 cm × 1 cm. NiFeV-LDH@CC was electrochemically activated by using cyclic voltammetry (CV) at a potential window of 1.042–1.642 V vs. RHE for 1000 cycles at a scan rate of 100 mV s^{-1} in 1 mol L^{-1} KOH solution. The compared samples were prepared as follows: The NiFe-LDH@CC sample on CC was synthesized by the same method as 2.2.1 without adding VCl_3. A-NiFe-LDH@CC was made from the electrochemical activation of NiFe-LDH@CC by the same method as 2.2.3. RuO_2 on CC was obtained by adding 2 mg of RuO_2 to 100 μL of ethanol and 100 μL of DI water and dissolve under ultrasonic. The solution was then added drop by drop onto the treated CC and dried at 60 °C overnight in vacuum. Pt/C-on-CC was synthesized by the same method as RuO_2-on-CC except that RuO_2 was replaced by 20% Pt/C.

2.3 Material characterization

The morphology and composition of the catalysts were obtained by LYRA3 XMH scanning electron microscope (SEM, TESCAN, Czech) and X-MaxN energy dispersive spectroscopy (EDS, Oxford Instruments). X-ray Photoelectron Spectroscopy (XPS) was performed on an Escalab 250Xi (Thermo Fisher Scientific, USA). X-ray diffraction (XRD) measurements were made using Ultima IV (Rigaku, Japan). A JEM F200 microscope (JEOL, Japan) is used to performed high-resolution transmission electron microscope (HRTEM). The metal concentration of the catalysts was detected using an inductively coupled plasma optical emission spectrometer (ICP-OES 720, Agilent, USA).

2.4 Electrochemical measurements

All electrochemical measurements were performed in a three-compartment electrochemical cell with a CHI 760e electrochemical workstation. Saturated Calomel Electrode (SCE) filled with saturated KCl solution was used as the reference electrode, while a carbon rod (Φ 6 mm) served as the counter electrode. The working electrode was a Pt electrode clip clamped CC filled with electrocatalysts with an working area of 1 cm × 1 cm. Electrochemical impedance spectroscopy (EIS) measurements were performed in the frequency range of 100 kHz to 0.01 Hz using an overpotential of 350 mV. Linear sweep voltammetry (LSV) polarization curves were obtained with 90% iR-compensation at a scan rate of 5 mV s^{-1}. Chronopotentiometry (CP) curves were recorded without iR-compensation at a constant current density of 10 mA cm^{-2}. All potentials described in this article were referred to as RHE and were transformed using the following equation: $E_{RHE}=E_{SCE}+0.2438+0.0591\times pH$. The overpotential ($\eta$) was derived using the formula: $\eta(V)=E_{RHE}-1.23V$. CV was used to probe the double layer capacitance (C_{dl}) of various samples at the non-Faradic region, which was identified at scan rates of 20, 40, 60, 80 and 100 mV s^{-1} in the range of 1.142–1.242 V vs RHE.

3 Results and discussion

SEM images of NiFeV-LDH@CC show that the nanosheets with the smooth and regular surface are vertically grown on CC to form the nanosheet arrays (Fig. S1a, b and Fig. 2a). After electrochemical activation, the overall morphology of the sample is not obviously changed, but the surface of the nanosheets becomes irregular and rough (Fig. S1c, d and Fig. 2d), indicating the surface reconstruction of NiFeV-LDH@CC. The TEM and HRTEM images of NiFeV-LDH@CC indicate that the edges of the nanosheets are straight with a corner angle of ~ 120° (Fig. 2b), which is characteristic of the crystal morphology of LDH[31]. Lattice spacings of 0.230 and 0.132 nm observed in Fig. 2c and Fig. S2b can be indexed to the planes of (015) and (119) of NiFe-LDH@CC (PDF: 40-0215). The TEM and HRTEM images of NiOOH/NiFeV-LDH@CC show that the edge of the nanosheets becomes much rougher and more irregular (Fig. 2e) than those of NiFeV-LDH@CC, and the lattice spacings of 0.203 and 0.230 nm in Fig. S2d and Fig. 2f can be corresponded to the (105) plane of NiOOH (PDF: 06-0075) and the (015) plane of NiFe-LDH@CC, respectively. In addition, the amorphous regions appear in the NiOOH/NiFeV-LDH@CC sample (marked with the red circles in Fig. 2f). The Fast Fourier Transform (FFT) images (Fig. S2b and d) derived from Fig. 2c, 2f demonstrate the appearance of new species on the surface of the nanosheet after electrochemical activation, which corresponds to the formation of the NiOOH phase. However, the crystal structure and morphology of the NiFe-LDH@CC sample without the addition of V are not obviously changed during the electrochemical activation (Fig. S3). The FFT images of NiFe-LDH@CC and A-NiFe-LDH@CC are similar, in which new species are not found. It can be inferred that adding V contributes to the appearance of the reconstructed NiOOH phase on the surface during electrochemical activation[29].

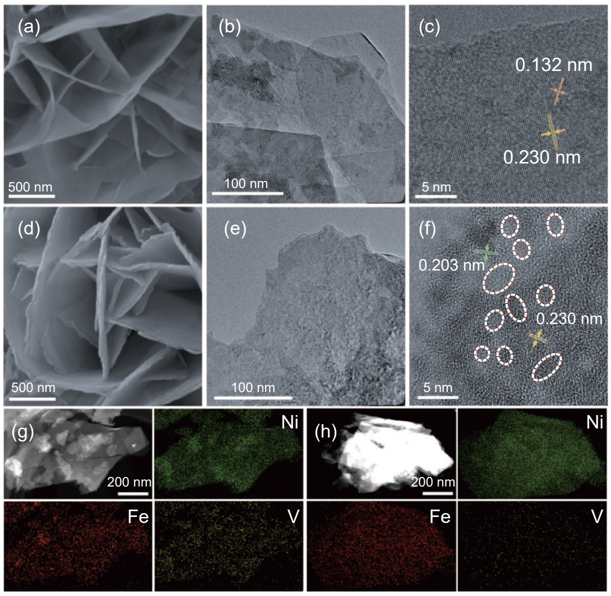

Fig. 2 SEM, TEM and HRTEM images of (a-c) NiFeV-LDH@CC and (d-f) NiOOH/NiFeV-LDH@CC. STEM-EDS mappings of (g) NiFeV-LDH@CC and (h) NiOOH/NiFeV-LDH@CC

XRD patterns of NiFeV-LDH@CC and NiOOH/NiFeV-LDH@CC show the peaks of CC at 25.5° and 43.4°, and a series of peaks of NiFe-LDH@CC at 11.5°, 23.1°, 33.5°, 34.5°, 39.0°, 46.0°, 60.0° and 61.2° for 2 samples, the peak of NiOOH is not observed in NiOOH/NiFeV-LDH@CC due to few crystalline NiOOH (Fig. 3a). Also, no pattern peak of V is found, indicating the successful doping of V, which partially replaces Fe sites after the hydrothermal process[32].

XPS was used to explore how electrochemical activation affected the chemical valence state and composition of NiFeV-LDH@CC. The XPS survey

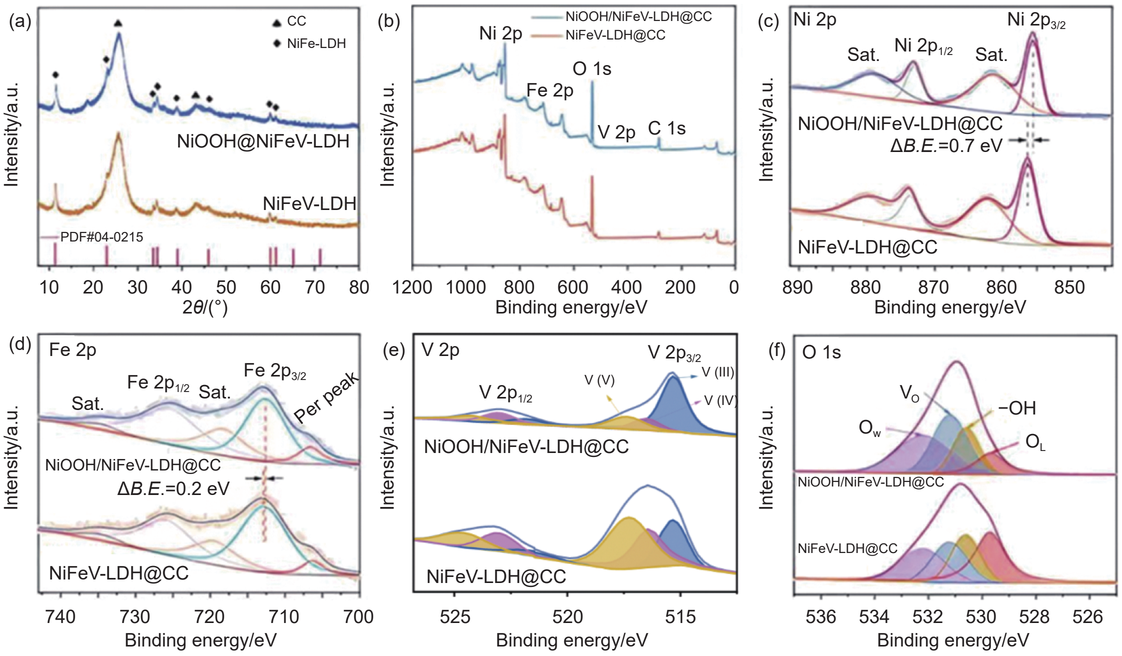

Fig. 3 (a) XRD patterns and (b) survey XPS Spectra of NiFeV-LDH@CC and NiOOH/NiFeV-LDH@CC. (c-f) Ni 2p, Fe 2p, V 2p and O 1s spectra of NiFeV-LDH@CC and NiOOH/NiFeV-LDH@CC

spectra of NiFeV-LDH@CC and NiOOH/NiFeV-LDH@CC show the presence of Ni, Fe, V and O in both samples (Fig. 3b). High-resolution Ni 2p spectra (Fig. 3c) show fitting peaks at 856.3 and 873.6 eV, which can be ascribed to Ni $2p_{3/2}$ and Ni $2p_{1/2}$ in NiFeV-LDH@CC respectively. After electrochemical activation, their fitting peaks shift to the lower side, as seen in NiOOH/NiFeV-LDH@CC. In the high-resolution Fe 2p spectra of NiFeV-LDH@CC and NiOOH/NiFeV-LDH@CC (Fig. 3d), fitting peaks at 712.6 and 725.4eV are ascribed to Fe $2p_{3/2}$ and Fe $2p_{1/2}$ of NiFeV-LDH@CC, which are slightly shifted to lower binding energy after electrochemical activation. The negative shift of the binding energy of Ni and Fe indicates the accumulation of electrons around Ni and Fe atoms due to the unsaturated metal sites with dangling bonds[33–34], caused by the increased V_O. The high-resolution V 2p spectra of NiFeV-LDH@CC and NiOOH/NiFeV-LDH@CC show that in addition to the obvious negative shift of the fitting peaks, the area integration of V 2p peak is decreased after electrochemical activation (Fig. 3e). It demonstrates an overall decrease in the valence and the content of V. Abundant V_V are formed in NiOOH/NiFeV-LDH@CC, the relative concentration of V_V rises markedly from 17.96% before reconstruction to 44.05% after, which are caused by the detachment of high valence V species from the lattice. The O 1s XPS spectra show peaks at 529.6, 530.6, and 532.2 eV which can be attributed to lattice oxygen (O_L), hydroxy species (—OH), and chemisorbed water (O_W) respectively (Fig. 3f). An additional peak at 531.2 eV is considered as coming from the O atoms in the vicinity of V_O[35]. The proportion of the integrated area of V_O increases from 21.36% to 39.24% after electrochemical activation. The XPS spectra of NiFe-LDH@CC and A-NiFe-LDH@CC without V doping show that the peak of V_O is not obviously changed and the binding energy of Ni and Fe atoms is not shifted after electrochemical activation (Fig. S4d-f). By comparing the results above it can be revealed that V doping has a significant impact on the formation of V_V and V_O due to the strong bonding between the higher valence V species (V^{4+}/V^{5+}) and O atoms in the lattice, and the good solubility of V-oxides (VO_2 and V_2O_5) in alkaline solutions[36–37].

SEM-EDS spectra in Fig. S5a,b reveal the uniform distribution of Ni, Fe, V and O elements throughout the NiFeV-LDH@CC and NiOOH/NiFeV-LDH@CC samples. It demonstrates that the relative atomic proportions of V and O are decreased, meaning that V and O are released from the lattice in the form of VO_2 and V_2O_5, generating a large number of V_V and V_O during electrochemical activation. ICP-OES was used to measure the metal contents. As shown in Table S1, the atomic ratio of Ni, Fe, and V in NiFeV-LDH@CC is 80.03 ∶ 13.11 ∶ 6.86, and that in NiOOH/NiFeV-LDH@CC is 80.87 ∶ 13.53 ∶ 5.6. The content of V is reduced after electrochemical activation, whereas Ni and Fe contents are not significantly changed. This observation aligns with the SEM-EDS outcome.

STEM-EDS was applied to further explore the distribution and content of elements on the nanosheets. As shown in Fig. 2g, h, the STEM-EDS spectra of NiFeV-LDH@CC and of NiOOH/NiFeV-LDH@CC show that the atomic ratio of Ni, Fe, and V in NiFeV-LDH@CC is 81.75 ∶ 12.03 ∶ 5.02, which is similar to the original feed ratio (Ni ∶ Fe ∶ V=16 ∶ 2 ∶ 1). After electrochemical activation, the atomic ratio of Ni, Fe and V of NiOOH/NiFeV-LDH@CC becomes 88.28 ∶ 11.56 ∶ 0.16. The ultra-low V content is due to the TEM specimen from the surface of NiOOH/NiFeV-LDH@CC during the ultrasonic separation, further proving the surface reconstruction caused by the V detachment to form the NiOOH active phase.

The formation of NiOOH is further confirmed by the CV curves of NiFeV-LDH@CC and NiFe-LDH@CC (Fig. S6a and c), showing that the oxidation peaks appear at about 1.4 V (vs. RHE) for both samples, which corresponds to the oxidation of Ni^{2+} to Ni^{3+}. Also, the heights of the oxidation peaks are increased until 1000 cycles for NiFeV-LDH@CC and 700 cycles for NiFe-LDH@CC, which indicates that the contents of NiOOH are increased with the CV cycles, and the content of NiOOH in NiFeV-LDH@CC is higher than that in NiFe-LDH@CC. The result indicates that the addition of V facilitates surface reconstruction to form the active NiOOH phase, which is also proven by color changes of the electrode (Fig. S7). Increasing the dose of added V from 0.125 to 0.25 mmol caused the thickness of the nanosheet array loaded onto CC reduces from 12.82 to 7.65 µm (Fig. S8). Increased acidity following the dissolution of VCl_3 severely limits the growth of NiFe-LDH@CC during the hydrothermal process, which is also reflected in the CV activation curves with a weaker tendency of the NiOOH formation (Fig. S6b).

The OER electrocatalytic performance of the obtained samples was assessed using the electrochemical method. LSV polarization curves in Fig. 4a and Fig. S10a show that NiOOH/NiFeV-LDH@CC achieves low overpotentials of 209 mV at 20 mA cm^{-2} (η_{20}) and 241 mV at 100 mA cm^{-2} (η_{100}), which are better than those of NiFeV-LDH@CC (η_{20}: 271 mV, η_{100}: 322 mV), A-NiFe-LDH@CC (η_{20}: 233 mV, η_{100}: 285 mV), NiFe-LDH@CC (η_{20}: 316 mV, η_{100}: 375 mV) and RuO_2@CC (η_{20}: 453 mV, η_{100}: 539 mV), visualized in Fig. 4b. Tafel plots (Fig. 4c) derived from the LSV curves also show a smaller value of 38 mV dec^{-1} for NiOOH/NiFeV-LDH@CC than those of NiFeV-LDH@CC (62 mV dec^{-1}), A-NiFe-LDH@CC (76 mV dec^{-1}) and NiFe-LDH@CC (63 mV dec^{-1}), which indicate that the NiOOH/NiFeV-LDH@CC electrode has faster kinetics for OER. The Electrochemical Surface Area (ECSA) is proportionate to the C_{dl} value. Therefore, CV curves were measured in the appropriate potential range without redox processes and the C_{dl} value was derived to determine the ECSA (Fig. S9). The results in Fig. 4d reveal that NiOOH/NiFeV-LDH@CC has a C_{dl} value of 2.21 mF cm^{-2}, which is higher than those of NiFeV-LDH@CC (0.26 mF cm^{-2}), A-NiFe-LDH@CC (2.10 mF cm^{-2}) and NiFe-LDH@CC (0.22 mF cm^{-2}). It implies that NiOOH/NiFeV-LDH@CC has larger ECSA, which partially facilitates the reaction. EIS measurements were performed to further study the kinetics of the as-obtained catalysts. The solution resistance (R_s) of all electrodes is ~ 2.0 Ω cm^2. The charge transfer resistance (R_{ct}) of NiOOH/NiFeV-LDH@CC (~ 0.54 Ω cm^2) is lower than that of NiFeV-LDH@CC (~ 0.70 Ω cm^2), A-NiFe-LDH@CC (~ 0.60 Ω cm^2) and NiFe-LDH@CC (~ 1.50 Ω cm^2). It demonstrates the fast electron transfer in the NiOOH/NiFeV-LDH@CC electrode. Long-term stability was investigated with

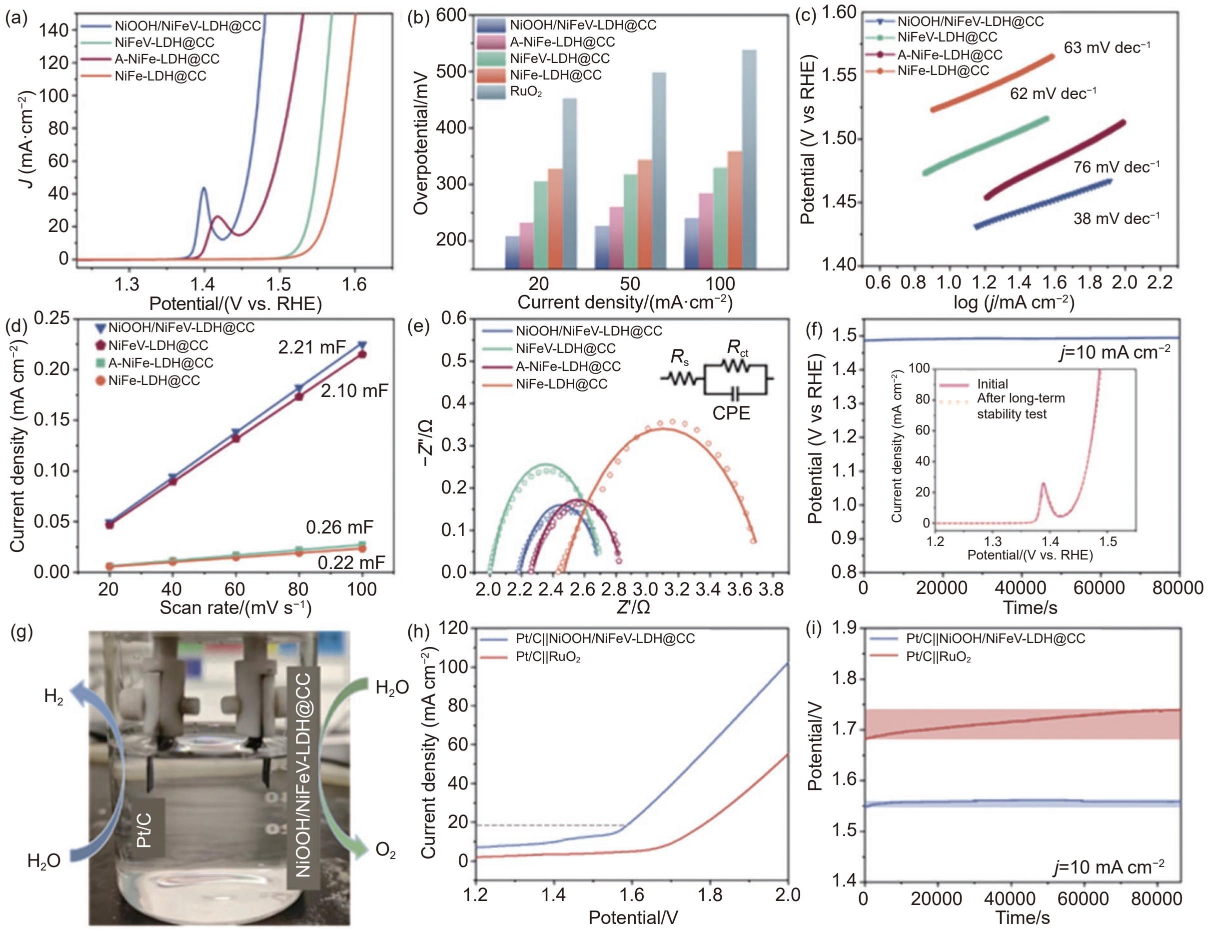

Fig. 4 (a) OER polarization curves. (b) Comparison of the overpotentials at different current densities. (c) Derived Tafel slopes. (d) C_{dl} plots. (e) EIS Nyquist plots measured at 350 mV overpotential for NiOOH/NiFeV-LDH@CC, NiFeV-LDH@CC, A-NiFe-LDH@CC and NiFe-LDH@CC. (f) CP test at 10 mA cm^{-2} of NiOOH/NiFeV-LDH@CC for 80 000 s (inset: LSV curves of NiOOH/NiFeV-LDH@CC before and after the stability test). (g) OWS composed of NiOOH/NiFeV-LDH@CC and Pt/C on CC. (h) OWS polarization curves and stability tests of Pt/C on CC || NiOOH/NiFeV-LDH@CC and Pt/C on CC || RuO_2

CP mode at a constant current density of 10 mA cm^{-2} for 80 000 s (Fig. 4f). Excellent oxygen evolution output is displayed by the NiOOH/NiFeV-LDH@CC electrode with no evident decline. Fig. 4g-i shows the over water splitting (OWS) cell assembled using Pt/C on CC and NiOOH/NiFeV-LDH@CC on CC as the cathode and anode, respectively. Compared to the Pt/C on CC || RuO_2-based electrolyzer, the Pt/C on CC || NiOOH/NiFeV-LDH@CC-based electrolyzer can drive a current density of 20 mA cm^{-2} under a much lower cell voltage of 1.597 V (without iR-compensation). This electrolyzer is stable, and drives a current density of 10 mA cm^{-2} at ~1.55 V for over 80 000 s without significant weakening.

After stability testing, as shown in the SEM image (Fig. 5a), the overall morphology of NiOOH/NiFeV-LDH@CC has not changed significantly. It remains as a nanosheet array with a rough surface and curled edges. In the TEM image (Fig. 5b, c), lattice spacings of 0.203 and 0.230 nm typical of NiOOH can still be observed on the surface of the NiFeV-LDH@CC nanosheets. The XRD pattern and XPS spetra of NiOOH/NiFeV-LDH@CC after stability testing show there is no obvious structural change (Fig. 5d) and the binding energy shift of Ni 2p and Fe 2p peaks (Fig. 5e-i). Further decreases in V content can be attributed to the dissolution of V species during OER in an alkaline environment over a long period of time. After stability testing, the content of V_O was 30.4%, which has not changed significantly.

We further investigated the formation process of NiOOH using in-situ Raman spectroscopy (Fig. S13). The results show that within the voltage range of

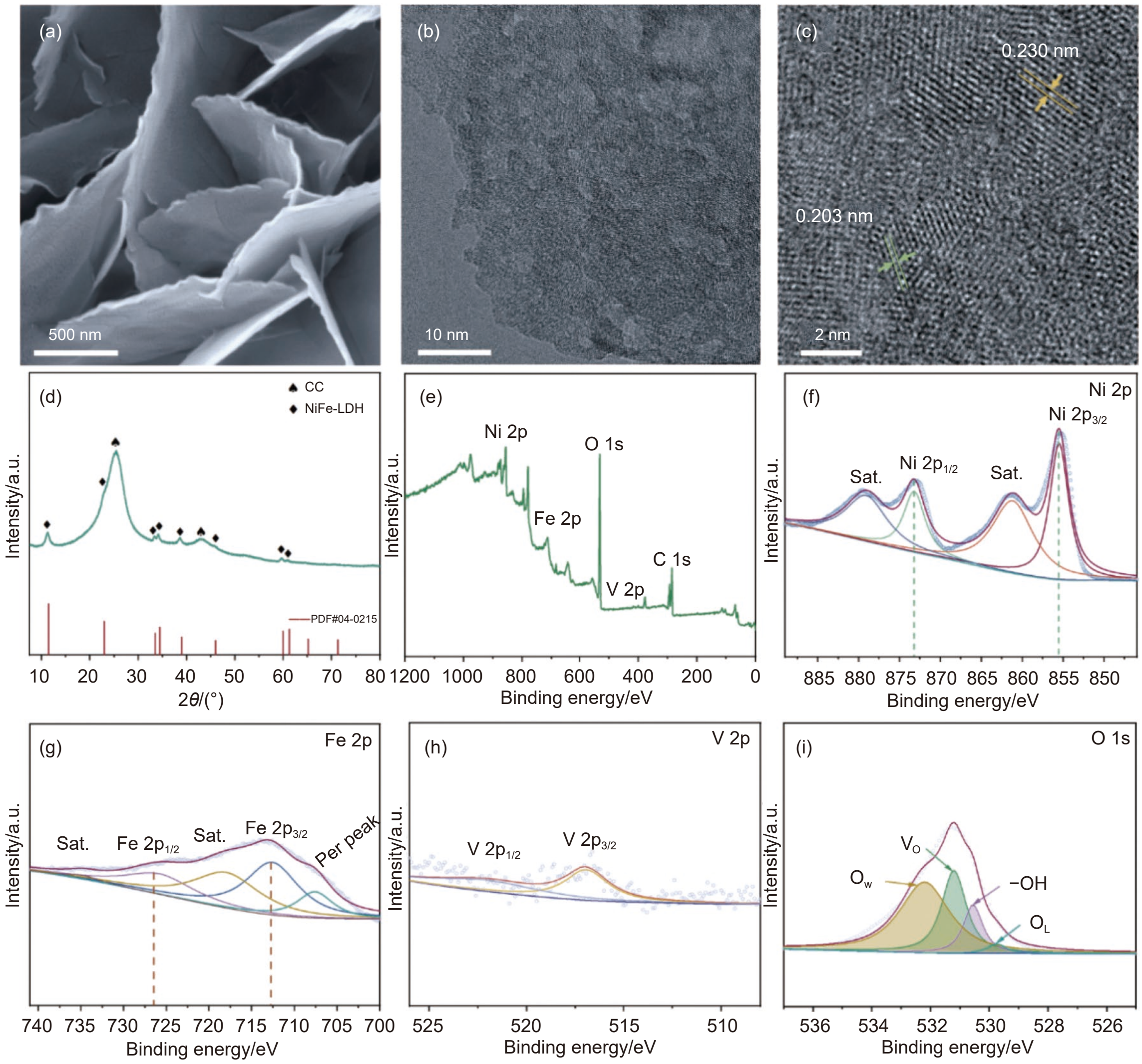

Fig. 5 (a) SEM, (b) TEM, (c) HRTEM image, (d) XRD pattern and (e) Survey XPS spectra of NiOOH/NiFeV-LDH@CC after stability testing. (f-i) High-resolution XPS spectra of Ni 2p, Fe 2p, V 2p, O 1s of NiOOH/NiFeV-LDH@CC after stability testing

1.1–1.3 V, only the characteristic peaks of NiFe-LDH are present. When the voltage increases to 1.4 V, peaks corresponding to NiFe-LDH disappear, and a new peak emerges at 558 cm^{-1}, confirming the formation of NiOOH. Additionally, in-situ Raman tests were performed on the compared sample $NiFeV_{0.25}$-LDH@CC. With increasing voltage, only the peaks of NiFe-LDH remain observable throughout, and no new peak appears. This finding aligns with our earlier hypothesis that excessive V content inhibits the reconstruction of NiOOH, resulting in surface signals too weak to be detected.

The overpotentials and Tafel slopes of the newly reported NiFe-based OER electrocatalysts in alkaline solution are shown in Table S2. The OER performance of NiOOH/NiFeV-LDH@CC is demonstrated to be on par with numerous first-rate non-noble metal catalysts. The excellent OER performance of the NiOOH/NiFeV-LDH@CC catalyst is due to the following reasons. Firstly the reconstructed NiOOH active phase caused by abundant V_V and V_O from the release of doped V during the electrochemical activation enhances the intrinsic activity of NiOOH/NiFeV-LDH@CC. Secondly, abundant V_O improves the electron distribution around the metal atoms and increases the electrical conductivity of NiOOH/NiFeV-LDH@CC.

4 Conclusions

In summary, NiOOH/NiFeV-LDH@CC catalyst with the structure of V-doped NiFe-LDH@CC nanosheet array on CC is obtained by a facile electrochemical activation, in which the reconstructed NiOOH phase as the actual active species is formed due to abundant V_V and V_O from the release of doped V. Benefiting from the improved intrinsic activity from the NiOOH active phase and the increased electrical conductivity from abundant V_O, NiOOH/NiFeV-LDH@CC exhibits excellent OER performance in 1 mol L^{-1} KOH solution, and only requires low overpotentials of 209 and 241 mV at 20 and 100 mA cm^{-2}, respectively. A straightforward method for reconstructing LDH surfaces is demonstrated. This method may be used to various LDH materials to enhance electrocatalytic performance.

Competing interests

We declare that the authors have no competing interests as defined by Springer, or other interests that might be perceived to influence the results and/or discussion reported in this paper.

Acknowledgements

This work was supported by National Natural Science Foundation of China (52572032, 52271064, 52571251, 52201019, U21A20174), Major Science and Technology Project of Shanxi Province (20201102003), Science and Technology Innovation Talent Team Project of Shanxi Province (202304051001010), Key National Scientific and Technological Cooperation Projects of Shanxi Province (202104041101008) and Natural Science Foundation of Shanxi Province (202203021211168, 202203021211138, 202303021221257). The authors acknowledge the assistance of Instrumental Analysis Center Taiyuan University of Technology.

References

[1] Xue B W, Zhang C H, Wang Y Z, et al. Recent progress of Ni–Fe layered double hydroxide and beyond towards electrochemical water splitting[J]. Nanoscale Advances, 2020, 2: 5555-5566.

[2] Jiao Y, Zheng Y, Jaroniec M, et al. Design of electrocatalysts for oxygen- and hydrogen-involving energy conversion reactions[J]. Chemical Society Reviews, 2015, 44: 2060-2086.

[3] Suen N T, Hung S F, Quan Q, et al. Electrocatalysis for the oxygen evolution reaction: recent development and future perspectives[J]. Chemical Society Reviews, 2017, 46: 337-365.

[4] Song Y, Liu P, Liu W, et al. Fe-doping induced localized amorphization in ultrathin a-Ni$(OH)_2$ nanomesh for superior oxygen evolution reaction catalysis[J]. Journal of Materials Chemistry A, 2021, 9: 14372-14380.

[5] Cherevko S, Geiger S, Kasian O, et al. Oxygen and hydrogen evolution reactions on Ru, RuO_2, Ir, and IrO_2 thin film electrodes in acidic and alkaline electrolytes: a comparative study on activity and stability[J]. Catalysis Today, 2016, 262: 170-180.

[6] Zeng F, Mebrahtu C, Liao LF, et al. Stability and deactivation of OER electrocatalysts: a review[J]. Journal of Energy Chemistry, 69: 301-329.

[7] McCrory CCL, Jung S, Ferrer IM, et al. Benchmarking hydrogen evolving reaction and oxygen evolving reaction electrocatalysts for solar water splitting devices[J]. Journal of the American Chemical Society, 2015, 137: 4347-4357.

[8] Shi Q, Zhu C, Du D, et al. Robust noble metal-based electrocatalysts for oxygen evolution reaction[J]. Chemical Society Reviews, 2019, 48: 3181-3192.

[9] Zhang Z, Zhang H, Zhang Z, et al. Interface engineering of porous $Co(OH)_2/La(OH)_3$@Cu nanowire heterostructures for high efficiency hydrogen evolution and overall water splitting[J]. Journal of Materials Chemistry A, 2023, 11: 4355-4364.

[10] Browne M P, Sofer Z and Pumera M. Layered and two dimensional metal oxides for electrochemical energy conversion[J]. Energy & Environmental Science, 2019, 12: 41-58.

[11] Kim J S, Kim B, Kim H, et al. Recent progress on multimetal oxide catalysts for the oxygen evolution reaction[J]. Advanced Energy Materials, 2018, 8: 1702774.

[12] Parra-Puerto A, Ng, K L, Fahy K, et al. Supported transition metal phosphides: activity survey for HER, ORR, OER, and corrosion resistance in acid and alkaline electrolytes[J]. ACS Catalysis, 2019, 9: 11515-11529.

[13] Dutta A and Pradhan N. Developments of metal phosphides as efficient OER precatalysts[J]. The Journal of Physical Chemistry Letters, 2016, 8: 144-152.

[14] Pu Z H, Liu T T, Amiinu I S, et al. Transition-metal phosphides: activity origin, energy-related electrocatalysis applications, and synthetic strategies[J]. Advanced Functional Materials, 2020, 30: 2004009.

[15] Wang Y, Kong B, Zhao D Y, et al. Strategies for developing transition metal phosphides as heterogeneous electrocatalysts for water splitting[J]. Nano Today, 2017, 15: 26-55.

[16] Chen R, Zhang Z, Wang Z, et al. Constructing air-stable and reconstruction-inhibited transition metal sulfide catalysts via tailoring electron-deficient distribution for water oxidation[J]. ACS Catalysis, 2022, 12: 13234-13246.

[17] Guo Y N, Park T, Yi J W, et al. Nanoarchitectonics for transition-metal-sulfide-based electrocatalysts for water splitting[J]. Advanced Materials, 2019, 31: 1807134.

[18] Li H, Chen S, Zhang Y, et al. Systematic design of superaerophobic nanotube-array electrode comprised of transition-metal sulfides for overall water splitting[J]. Nature Communications, 2018, 9: 1-12.

[19] Burke M S, Enman L J, Batchellor A S, et al. Oxygen evolution reaction electrocatalysis on transition metal oxides and (Oxy)hydroxides: activity trends and design principles[J]. Chemistry of Materials, 2015, 27: 7549-7558.

[20] Dionigi F, Zhu J, Zeng Z, et al. Intrinsic electrocatalytic activity for oxygen evolution of crystalline 3d-transition metal layered double hydroxides[J]. Angewandte Chemie International Edition, 2021, 60: 14446-14457.

[21] Han J and Guan J. Multicomponent transition metal oxides and (oxy)hydroxides for oxygen evolution[J]. Nano Research, 2022, 16: 1913-1966.

[22] Song Y, Xu B, Liao T, et al. Electronic structure tuning of 2d metal (Hydr)oxides nanosheets for electrocatalysis[J]. Small, 2020, 17: 2002240.

[23] Bodhankar P M, Sarawade P B, Singh G, et al. Recent advances in highly active nanostructured NiFe LDH catalyst for electrochemical water splitting[J]. Journal of Materials Chemistry A, 2021, 9: 3180-3208.

[24] Gong L, Yang H, Douka A I, et al. Recent progress on NiFe-based electrocatalysts for alkaline oxygen evolution[J]. Advanced Sustainable Systems, 2020, 5: 2000136.

[25] Zhang K and Zou R Advanced transition metal-based OER electrocatalysts: current status, opportunities, and challenges[J]. Small, 2021, 17: 2100129.

[26] Trotochaud L, Young S L, Ranney J K, et al. Nickel–iron oxyhydroxide oxygen-evolution electrocatalysts: the role of intentional and incidental iron incorporation[J]. Journal of the American Chemical Society, 2014, 136: 6744-6753.

[27] Zhai Y, Ren X, Sun Y, et al. Synergistic effect of multiple vacancies to induce lattice oxygen redox in NiFe-layered double hydroxide OER catalysts[J]. Applied Catalysis B: Environmental, 2023, 323: 122091.

[28] Chen T, Li B, Song K, et al. Defect-activated surface reconstruction: mechanism for triggering the oxygen evolution reaction activity of NiFe phosphide[J]. Journal of Materials Chemistry A, 2022, 10: 22750-22759.

[29] Wu Y, Yang J, Tu T, et al. Evolution of cationic vacancy defects: a motif for surface restructuration of OER precatalyst[J]. Angewandte Chemie International Edition, 2021, 60: 26829-26836.

[30] Zeng Y, Zhao M, Huang Z, et al. Surface reconstruction of water splitting electrocatalysts[J]. Advanced Energy Materials, 2022, 12: 2270141.

[31] Zhao J W, Shi Z X, Li C F, et al. Boosting the electrocatalytic performance of NiFe layered double hydroxides for the oxygen evolution reaction by exposing the highly active edge plane (012)[J]. Chemical Science, 2021, 12: 650-659.

[32] Li P, Duan X, Kuang Y, et al. Tuning electronic structure of NiFe layered double hydroxides with vanadium doping toward high efficient electrocatalytic water oxidation[J]. Advanced Energy Materials, 2018, 8: 1704431.

[33] Jiao S, Yao Z, Li M, et al. Accelerating oxygen evolution electrocatalysis of two-dimensional NiFe layered double hydroxide nanosheets via space-confined amorphization[J]. Nanoscale, 2019, 11: 18894.

[34] Zhou D, Wang S, Jia Y, et al. NiFe hydroxide lattice tensile strain: enhancement of adsorption of oxygenated intermediates for efficient water oxidation catalysis[J]. Angewandte Chemie International Edition, 2018, 58: 736-740.

[35] Li Q, Huang F, Li S, et al. Oxygen vacancy engineering synergistic with surface hydrophilicity modification of hollow Ru doped CoNi-LDH nanotube arrays for boosting hydrogen evolution[J]. Small, 2022, 18: 2104323.

[36] Fan K, Ji Y, Zou H, et al. Hollow iron–vanadium composite spheres: a highly efficient iron-based water oxidation electrocatalyst without the need for nickel or cobalt[J]. Angewandte Chemie International Edition, 2017, 56: 3289-3293.

[37] Fan K, Zou H, Duan L, et al. Selectively etching vanadium oxide to modulate surface vacancies of unary metal–based electrocatalysts for high-performance water oxidation[J]. Advanced Energy Materials, 2019, 10: 1903571.